actuators

MDPI

Article

Universal Model and Control Framework for Bearingless Motors with Combined Windings

Takahiro Noguchi [1,*], Mohamadhasan Mokhtarabadi [1], Kamisetti N. V. Prasad [1], David Prinz [2], Wolfgang Gruber [3] and Eric L. Severson [1]

[1] Department of Mechanical Engineering, University of Minnesota, 111 Church St SE, Minneapolis, MN 55455, USA; mokht029@umn.edu (M.M.); fkamiset@umn.edu (K.N.V.P.); sever@umn.edu (E.L.S.)
[2] Linz Center of Mechatronics GmbH, Altenberger Str. 69, 4040 Linz, Austria; david.prinz@lcm.at
[3] Institute of Electric Machines and Power Electronics, Johannes Kepler University Linz, Altenberger Str. 69, 4040 Linz, Austria; wolfgang.gruber@jku.at
* Correspondence: tnoguchi@umn.edu

Abstract

This paper presents a model and control framework for bearingless motors that is generalized for all types of combined-winding configurations with six phases. The aim of the paper is to facilitate the rapid implementation of MATLAB Simulink models of the electric behavior (voltage/current) and mechanical behavior (force/torque) of radial-flux, non-salient bearingless motors with combined windings. Bearingless motor developers will find this to be a useful guide for creating control simulations and understanding how changes in the number of motor/suspension poles and winding type impact their control architecture. The paper shows how the provided universal model/controller can serve as the starting point and baseline for establishing a control simulation environment that is later refined to capture the architecture-specific aspects of a practical bearingless motor control system. A case-study machine with a $p = 7$ motor and $p_s = 8$ suspension pole-pairs is introduced and the universal controller concept is validated through simulation and experimental results.

Keywords: bearingless motor; combined winding; DPNV winding; space vector; Simulink; winding functions

Check for updates

Academic Editors: Satoshi Ueno, Toshihiko Sugiura and Junichi Asama

Received: 27 May 2026
Revised: 16 July 2026
Accepted: 21 July 2026
Published: 24 July 2026

Copyright: © 2026 by the authors. Licensee MDPI, Basel, Switzerland. This article is an open access article distributed under the terms and conditions of the Creative Commons Attribution (CC BY) license.

1. Introduction

Bearingless motor development has historically been relegated to highly targeted, isolated applications with extreme need for magnetic levitation. This includes implantable blood pumps [1–3], hygienic mixing devices [4–6], and flywheel energy storage [7–9]. The wide variety of applications of differing needs has led to a fragmented approach to developing this technology: researchers investigate a unique machine topology, with a unique model and control requirements, as if it is an isolated invention. More recently, efforts have been underway to develop bearingless motors for industrial-scale applications [10–12], which has resulted in publications generalizing the theory, advancements, and converter sizing considerations behind bearingless motors.

Generalized theory for studying force behavior in bearingless motors has been developed and summarized in [13–17]. The impact of eddy currents on bearingless motor force capability is studied in [15], and design rules are established to achieve high force performance with minimal vector error through optimal pole-pair selection and by limiting allowable stator-winding field harmonics in [13,17]. In [18], the theoretical foundation of

combined-winding configurations was reviewed and unified using generalized winding functions. Reference [19] presented a generalized winding design methodology for arbitrary slot-and-pole combinations for combined windings. A general control strategy based on dual field-oriented control was introduced in [20] and a technique to rapidly calculate combined-winding current commands from force commands was developed in [21]. Other studies have investigated application-specific aspects using combined windings, e.g., quantifying performance advantages of using combined windings over separated windings [22,23], machine design methodologies for bearingless slice motors [24,25], topology comparisons for high-speed bearingless drives [26], fault-tolerant control [27], and suspension converter sizing for different winding configurations [28]. This paper continues the trend of unifying the modeling and control approaches for bearingless motors.

The primary contribution of this paper is to provide a generalized model for radial-flux, non-salient bearingless motors with six phases using any combined-winding configuration. The proposed framework assumes ideal sinusoidal winding functions and is applicable to $p_s = p \pm 1$ bearingless machines, where p is the number of pole-pairs of the motor, and p_s is the number of pole-pairs of the suspension winding. The windings considered in this paper include multiphase (MP), multiphase with a dual neutral point (DNMP), bridge and parallel dual-purpose no-voltage (DPNV), and mid-point current injection (MCI). The paper reviews the literature on these configurations and highlights the following recent advancements: (1) all combined windings can be realized with the same stator-winding pattern, but with different drive connections and control architectures; and (2) from this universal winding pattern, generalized winding functions can be expressed for each phase of the combined winding. The paper uses these generalized winding functions to create a general inductance matrix and force/torque expressions and shows how these can be combined to model the complete machine. This facilitates the development of a MATLAB Simulink model generalized to all winding types that can be configured at runtime via a script that specifies the number of pole-pairs and winding type.

The proposed framework allows bearingless motor engineers to simulate and develop control strategies for a wide range of bearingless motor configurations using a single flexible Simulink template. The paper includes a case study to demonstrate the generalized modeling approach and provides a Simulink template that readers can download via an open-source GitHub repository: https://github.com/severson-group/bm-modeling (accessed on 22 May 2026). This paper is extended from a conference version published in [29]. The additional contribution includes experimental validation of the proposed universal controller using a case-study machine.

2. Multiphase Combined-Winding Bearingless Motor Model

This section reviews and formulates the complete bearingless motor model for MP windings. As shown in [19], MP combined windings are the most general form of combined winding and all other combined-winding types can be understood as special cases of the MP winding. Later, Section 3 uses the results of this section to propose the paper's universal combined-winding bearingless motor model.

This section derives force/torque and electrical (voltage, current, inductance) expressions. The derivation starts from fundamentals by using both the well-known winding function theory [30] (Chapter 1) to make airgap field calculations and the Maxwell stress tensor to derive force and torque.

2.1. Airgap Field Calculations

Recent studies [18,19] have shown that the idealized phase winding functions for all types of combined-winding bearingless motors must be as follows:

$$N_k(\alpha) = \hat{N}_p \cos\left(p\alpha - \alpha_{w0,p} - [k-1]\alpha_t\right) + \hat{N}_{p_s} \cos\left(p_s\alpha - \alpha_{w0,p_s} - [k-1]\alpha_s\right), \quad (1)$$

where $\hat{N}_p$ is the torque-winding function amplitude, $\hat{N}_{p_s}$ is the suspension-winding function amplitude, α is an arbitrary angular location in the airgap, and k indicates the phase number. The offset angles $\alpha_{w0,p}$ and α_{w0,p_s} are included for generality in Equation (1), but are neglected for simplicity in this paper. It is a critical result of these articles that α_s and α_t are uniquely determined by the pole-pair combination as

$$\alpha_t = \text{wrap}\left(p\frac{2\pi}{m}\right), \qquad \alpha_s = \text{wrap}\left(p_s\frac{2\pi}{m}\right), \quad (2)$$

where m denotes the number of phases and the right hand side is wrapped between $-\pi$ and π rad. This paper will consider only $m = 6$-phase machines. Each phase of the winding produces a radial and tangential field. It is well known from winding function theory that the radial field can be calculated as $B_w = \mu_0 \frac{N_k(\alpha) i_k}{\delta}$ and that a winding function harmonic n of the form $N_n(\alpha) = \hat{N}_n \cos(n\alpha - \gamma)$ will also produce a tangential field of $B_{n,\tan}(\alpha) = -\mu_0 \frac{n\hat{N}_n}{r} i_k \sin(n\alpha - \gamma)$ when excited with current i_k, where r is the airgap radius and γ is the angular location of the magnetic field produced by the winding. This paper assumes a magnetizing airgap field of $B_\delta(\alpha) = \hat{B}_\delta \cos(p\alpha - \theta)$ in the radial direction, where $\theta = p\theta_{mech}$ and θ_{mech} is defined in Figure 1 for a permanent magnet rotor.

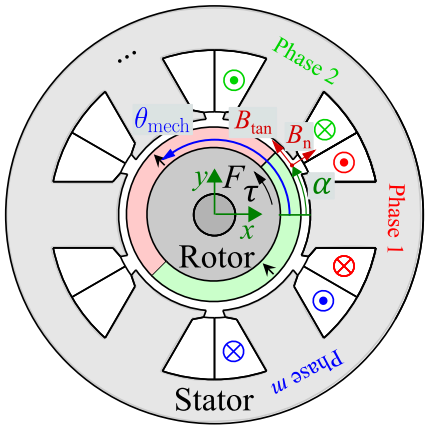


Figure 1. PM motor cross-section with the definitions of axes and field components.

2.2. Force and Torque Model

The airgap fields derived in Section 2.1 are now used with the Maxwell stress tensor to determine the force and torque that each phase winding creates on the shaft, as follows:

$$\begin{bmatrix} \sigma_n \\ \sigma_{tan} \end{bmatrix} = \begin{bmatrix} \frac{1}{2\mu_0}(B_n^2 - B_{tan}^2) \\ \frac{1}{\mu_0} B_n B_{tan} \end{bmatrix} \quad \Rightarrow \quad F_x \approx \frac{rl}{2\mu_0}\int_0^{2\pi} {B_n}^2 \cos\alpha \mathrm{d}\alpha, \; F_y \approx \frac{rl}{2\mu_0}\int_0^{2\pi} {B_n}^2 \sin\alpha \mathrm{d}\alpha, \; \tau = \frac{rl}{\mu_0}\int_0^{2\pi} B_n B_{tan} \mathrm{d}\alpha. \quad (3)$$

Here, σ_n and σ_{tan} are the normal and tangential components of the Maxwell stress acting on the surface of the rotor, l is the axial length of the rotor, and B_{tan}^2 is considered negligibly small, assuming the squared tangential flux density is much smaller than the squared radial flux density, i.e., $B_n^2 \gg B_{tan}^2$. When used with the winding function (Equation (1)) and field expressions from Section 2.1, each phase winding is found to produce the following form of force and torque:

$$F_{x,k} = \hat{f} i_k \cos(\theta - [k-1]\alpha_s), \qquad F_{y,k} = \mp \hat{f} i_k \sin(\theta - [k-1]\alpha_s), \qquad \tau = -\hat{\tau} i_k \sin(\theta - [k-1]\alpha_t), \quad (4)$$

where $F_{y,k}$ is negative for $p_s = p+1$ and positive for $p_s = p-1$. While $\hat{f}$ and $\hat{\tau}$ can be calculated analytically from Equation (3), it is common to determine these from finite element analysis or hardware measurements, e.g., [31].

It is common practice to present the force/torque model in the form $[F_x, F_y, \tau]^\top = \mathbf{T}_m(\theta)\mathbf{i}_m + \mathbf{M}_c(\theta)$, as described in [24]. The $\mathbf{M}_c$ matrix captures cogging force and torque of the machine and is independent of current. The phase currents are represented as the vector $\mathbf{i}_m = [i_1, i_2, i_3, i_4, i_5, i_6]^\top$. The $\mathbf{T}_m$ matrix is composed of the force and torque expressions in Equation (4) and is depicted in Figure 2 for different pole combinations, which correspond to different α_s and α_t values, as calculated by Equation (2).

When the phase winding currents are of the form of Equation (5) (see [18]) (Equation (10)), the resulting shaft force and torque are calculated as Equation (6), where F_y is positive for $p_s = p+1$ and negative for $p_s = p-1$.

$$i_k = \hat{I}_t \cos\left(\theta + \phi_t' - [k-1]\alpha_t\right) + \hat{I}_s \cos\left(\theta + \phi_s' - [k-1]\alpha_s\right) \tag{5}$$

$$F_x = k_f \hat{I}_s \cos\phi_s', \;\; F_y = \pm k_f \hat{I}_s \sin\phi_s', \;\; \tau = k_t \hat{I}_t \sin\phi_t', \qquad \text{where: } k_f = 3\hat{f},\; k_t = 3\hat{\tau} \tag{6}$$

where ϕ_t' and ϕ_s' denote the phase angles of the torque and suspension current vectors, respectively. For example, $\phi_t' = \pi/2$ corresponds to a pure q-axis current in the torque current space vector introduced in Section 2.4.

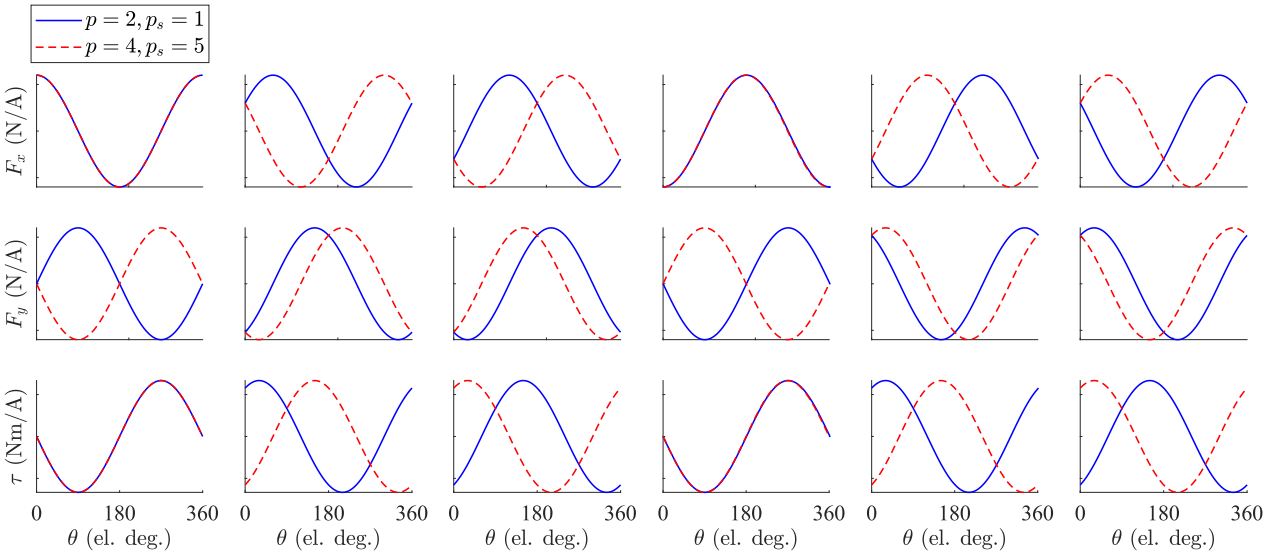


Figure 2. $\mathbf{T}_m$ matrix for $p = 2$, $p_s = 1$ and $p = 4$, $p_s = 5$ bearingless machines.

2.3. Electric Model

The electrical model equations (inductance, back-EMF) are now derived for the winding. The EMF induced in each phase due to the magnetizing field can be calculated using the phase winding function (Equation (1)) as follows:

$$\lambda_k(\theta) = rl\int_0^{2\pi} N_k(\alpha)B_\delta(\alpha)\mathrm{d}\alpha = \underbrace{\pi\hat{N}_p\hat{B}_\delta rl}_{k_e}\cos(\theta - [k-1]\alpha_t) \quad \Rightarrow \quad e_k = \frac{d\lambda_k}{dt} = k_e\omega\sin([k-1]\alpha_t - \theta) \tag{7}$$

The inductance of each phase winding can be similarly calculated using winding function theory as

$$L_{j,k} = \mu_0\frac{rl}{\delta}\int_0^{2\pi} N_j(\alpha)N_k(\alpha)\mathrm{d}\alpha = \tfrac{1}{3}[L_t\cos([k-j]\alpha_t) + L_s\cos([k-j]\alpha_s)], \tag{8}$$

where $L_t = 3L_0\hat{N}_p^2$, $L_s = 3L_0\hat{N}_{p_s}^2$, and $L_0 = \mu_0\pi\frac{rl}{\delta}$ are common term pairings, e.g., [18] (Equation (29)).

These expressions enable the development of a complete winding electric model of $\mathbf{v}_m = \mathbf{R}\mathbf{i}_m + \mathbf{L}\frac{d}{dt}\mathbf{i}_m + \mathbf{e}_m$, where $\mathbf{e}_m$ is the column vector populated by Equation (7) and the inductance matrix is of the form:

$$\mathbf{L} = \frac{1}{3}\begin{pmatrix} L_t + L_s & L_t\cos\alpha_t + L_s\cos\alpha_s & L_t\cos(2\alpha_t) + L_s\cos(2\alpha_s) & \cdots \\ L_t\cos\alpha_t + L_s\cos\alpha_s & L_t + L_s & L_t\cos\alpha_t + L_s\cos\alpha_s & \cdots \\ L_t\cos(2\alpha_t) + L_s\cos(2\alpha_s) & L_t\cos\alpha_t + L_s\cos\alpha_s & L_t + L_s & \cdots \\ \vdots & \vdots & \vdots & \ddots \end{pmatrix} \tag{9}$$

2.4. Space Vector Model

It is well known that the Generalized Clarke Transformation (GCT) can be used to transform the voltage and current expressions into space vector equations to yield a compact notation for describing the models developed in Sections 2.2 and 2.3 [18]. This transformation is applied to the current expression (Equation (5)) to obtain the following space vectors associated with torque and suspension current.

$$\vec{f}_t = f_{\alpha_t} + jf_{\beta_t} = c\sum_{k=1}^{m} f_k e^{j[k-1]\alpha_t},\ \vec{f}_s = f_{\alpha_s} + jf_{\beta_s} = c\sum_{k=1}^{m} f_k e^{j[k-1]\alpha_s} \quad \Rightarrow \quad \vec{i}_t = \hat{I}_t e^{j\theta+\phi'_t},\ \vec{i}_s = \hat{I}_s e^{j\theta+\phi'_s} \text{ for } c = \tfrac{1}{3} \tag{10}$$

The space vectors can be rotated by θ into the synchronous frame as $\vec{i}_t^{\,T} = \vec{i}_t e^{-j\theta} = \hat{I}_t e^{j\phi'_t}$ and $\vec{i}_s^{\,S} = \vec{i}_s e^{-j\theta} = \hat{I}_s e^{j\phi'_s}$. Using Equation (6), these space vectors can be conveniently connected to shaft torque and force as follows:

$$\begin{aligned} \vec{T} &= T_d + j\tau = k_t\vec{i}_t^{\,T} = \bar{k}_t\vec{i}_t && \text{where } \bar{k}_t = k_t e^{-j\theta} \text{ and } \vec{i}_t^{\,T} = i_d + ji_q \\ \vec{F} &= F_x + jF_y, \quad \begin{matrix} p_s = p+1: & F_x + jF_y \\ p_s = p-1: & F_x - jF_y \end{matrix} \Big\} = k_f\vec{i}_s^{\,S} = \bar{k}_f\vec{i}_s && \text{where } \bar{k}_f = k_f e^{-j\theta} \text{ and } \vec{i}_s^{\,S} = i_x + ji_y \end{aligned} \tag{11}$$

where T_d is the flux-weakening component.

The GCT can be similarly applied to the electric model of Section 2.3 to arrive at

$$\vec{v}_t = L_t\tfrac{d}{dt}\vec{i}_t + R\vec{i}_t + \vec{e}_m, \qquad \vec{v}_s = L_s\tfrac{d}{dt}\vec{i}_s + R\vec{i}_s \tag{12}$$

3. Proposed Universal Model

In addition to multiphase combined windings, researchers have independently developed three other types of combined windings, namely bridge DPNV [32,33], parallel DPNV [34], and mid-point current injection [35] configurations, as shown in Figure 3. It was shown in [19] that these winding types are actually multiphase windings where the phases are connected to the drive electronics in unique configurations depending on the distinct objective (i.e., eliminate back-EMF at the suspension inverter). This means that the force/torque and electric models for these windings can be derived from the multiphase winding. Such derivations are provided in [18] (Table I) and [36] (Section V).

This section summarizes the equivalencies of combined windings, presents transformation matrices between winding types, and proposes the paper's universal model that is applicable to all combined-winding bearingless motors.

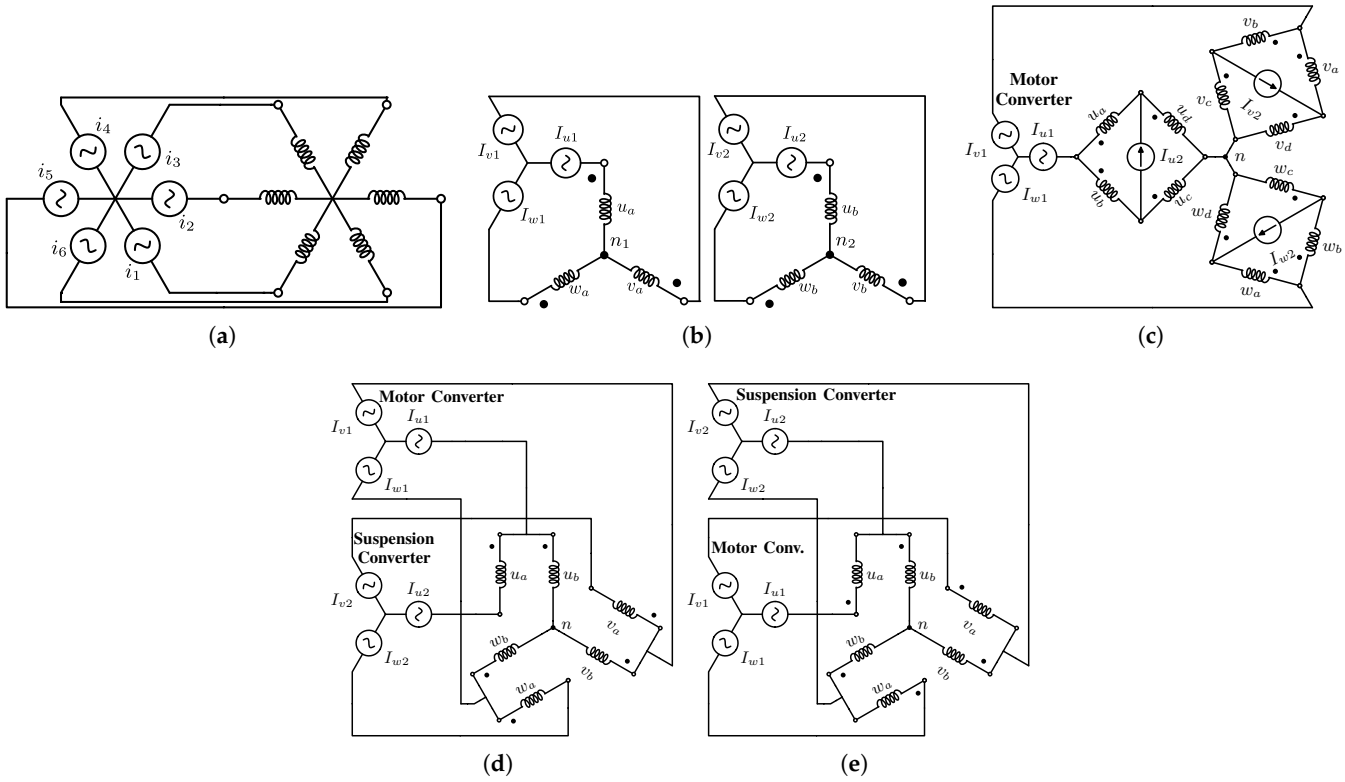


Figure 3. Combined windings: (**a**) multiphase winding with single neutral point (MP), (**b**) multiphase winding with dual neutral point (DNMP), (**c**) bridge DPNV, (**d**) parallel DPNV, and (**e**) MCI.

3.1. Transformation to Combined Winding Using Space Vector Model

To create the torque and force indicated in Equation (6), the bridge DPNV, parallel DPNV and MCI drives must (1) control currents in the MP phases, as described in Equation (5), and (2) connect the MP winding phases to the drive electronics in the manner shown in Figure 3. To accomplish this, a deliberate assignment must be made of the MP phases (phase 1, 2, ...6) to the coil group labels of "u_a", "u_b", etc., shown in Figure 3, as described in [18] (Table I) and summarized later in Table 5.

The windings must control the terminal currents listed in Table 2, where $\vec{i}_{\mathrm{t}}$ and $\vec{i}_{\mathrm{s}}$ are the space vectors calculated in Equation (10). The superscript * indicates a complex conjugate and the subscript $_{\mathrm{term}}$ indicates the terminal current space vectors, which correspond to the currents entering the three-phase "motor" and "suspension" terminals in Figure 3 using the standard three-phase Clarke Transform. Notice that the space vector model to control these windings has been developed in the literature in a similar form to Equations (11) and (12), but described from the perspective of each winding's terminal currents and voltages. In this case, the suspension current vector $\vec{i}_{\mathrm{s},w}$ rotates in the opposite direction to the torque current vector $\vec{i}_{\mathrm{t},w}$, as indicated by the complex conjugate in the "Control Currents" row (see Table 2). This difference in rotation direction must be carefully considered to calculate shaft torque and force in Equation (13), where two different force vectors are defined depending on whether $p_{\mathrm{s}} = p + 1$ or $p_{\mathrm{s}} = p - 1$. In Equation (13), $\bar{k}_{\mathrm{t},w}$, $\bar{k}_{\mathrm{f},w}$, $\vec{i}_{\mathrm{t},w}$, and $\vec{i}_{\mathrm{s},w}$ are the machine parameters found in the literature for these windings, while $\vec{i}_{\mathrm{t}}^{\,\mathrm{T}}$ and $\vec{i}_{\mathrm{s}}^{\,\mathrm{S}}$ remain the synchronous-frame space vectors used in Equation (11). Notice that the y-direction force is reversed as compared to Equation (11); this is a consequence of $\vec{i}_{\mathrm{s},w}$ rotating in the $-\theta$ direction. To clarify this sign convention of the y-direction force, Table 1 summarizes the force expressions in Equations (11) and (13). Using the force expression $F_{\mathrm{x}} + jF_{\mathrm{y}}$ in the MP winding row and the $p_{\mathrm{s}} = p + 1$ column of Table 1 as the references, the direction of the generated force along the y-axis is reversed if: (1) the bearingless machine pole-pair

combination is $p_s = p - 1$ or (2) the conjugate of the suspension current space vector $\vec{i}_s^{S*}$ is used, which is a characteristic of circuit-based combined windings.

$$\begin{aligned} \vec{T} &= T_d + j\tau = k_t \vec{i}_t^{T} = \bar{k}_{t,w} \vec{i}_{t,w} && && \text{using } \bar{k}_{t,w} \text{ and } \vec{i}_{t,w} \text{ from Table 2} \\ \vec{F} &= F_x + jF_y, && \left.\begin{matrix} p_s = p+1: & F_x - jF_y \\ p_s = p-1: & F_x + jF_y \end{matrix}\right\} = k_f \vec{i}_s^{S*} = \bar{k}_{f,w} \vec{i}_{s,w} && \text{using } \bar{k}_{f,w} \text{ and } \vec{i}_{s,w} \text{ from Table 2} \end{aligned} \tag{13}$$

Table 1. Force vector definitions for different pole-pair combinations and winding configurations.

	Machine Design	
Winding Configuration/Controlled Suspension Current	$p_s = p+1$	$p_s = p-1$
MP winding, $\vec{i}_s^{S}$ (see Equation (11))	$F_x + jF_y$	$F_x - jF_y$
Circuit-based combined windings, $\vec{i}_s^{S*}$ (see Equation (13))	$F_x - jF_y$	$F_x + jF_y$

Terminal and control voltage vectors in Tables 2 and 3 relate electric models reported in the literature to the MP electric model. These differential equations are used to design current regulators to control force and torque. Effective controller design (particularly of feedforward decoupling terms) has been the subject of several papers, e.g., [37].

Table 2. Space vector model of the circuit-based combined windings in terms of the MP winding quantities.

	DNMP	**Bridge DPNV**	**Parallel DPNV**	**MCI**
Terminal Currents	$\vec{i}_{1,term} = \vec{i}_t - \vec{i}_s^*$ $\vec{i}_{2,term} = \vec{i}_t + \vec{i}_s^*$	$\vec{i}_{t,term} = 2\vec{i}_t$ $\vec{i}_{s,term} = 2\vec{i}_s^*$	$\vec{i}_{t,term} = 2\vec{i}_t$ $\vec{i}_{s,term} = -\vec{i}_t + \vec{i}_s^*$	$\vec{i}_{t,term} = \vec{i}_t - \vec{i}_s^*$ $\vec{i}_{s,term} = 2\vec{i}_s^*$
Control Currents $\vec{i}_{t,w}$, $\vec{i}_{s,w}$	$\vec{i}_{t,DNMP} = \vec{i}_t$ $\vec{i}_{s,DNMP} = \vec{i}_s^*$	$\vec{i}_{t,B} = 2\vec{i}_t \quad \vec{i}_{s,B} = 2\vec{i}_s^*$	$\vec{i}_{t,P} = 2\vec{i}_t \quad \vec{i}_{s,P} = \vec{i}_s^*$	$\vec{i}_{t,MCI} = \vec{i}_t$ $\vec{i}_{s,MCI} = 2\vec{i}_s^*$
Torque $\bar{k}_{t,w}$	$\bar{k}_{t,DNMP} = k_t e^{-j\theta}$	$\bar{k}_{t,B} = \frac{k_t}{2} e^{-j\theta}$	$\bar{k}_{t,P} = \frac{k_t}{2} e^{-j\theta}$	$\bar{k}_{t,MCI} = k_t e^{-j\theta}$
Force $\bar{k}_{f,w}$	$\bar{k}_{f,DNMP} = k_f e^{j\theta}$	$\bar{k}_{f,B} = \frac{k_f}{2} e^{j\theta}$	$\bar{k}_{f,P} = k_f e^{j\theta}$	$\bar{k}_{f,MCI} = \frac{k_f}{2} e^{j\theta}$

Table 3. Terminal and control voltage equations.

	Torque	**Suspension**
DNMP	$\vec{v}_{1,term} = \overbrace{L_t \frac{d}{dt}\vec{i}_{t,DNMP} + R\vec{i}_{t,DNMP} + \vec{e}_m}^{\vec{v}_{t,DNMP}} \overbrace{- R\vec{i}_{s,DNMP} - L_s \frac{d}{dt}\vec{i}_{s,DNMP}}^{\text{cross-coupling}}$	$\vec{v}_{2,term} = \overbrace{L_s \frac{d}{dt}\vec{i}_{s,DNMP} + R\vec{i}_{s,DNMP} + \vec{e}_m}^{\vec{v}_{s,DNMP}} + \overbrace{R\vec{i}_{t,DNMP} + L_t \frac{d}{dt}\vec{i}_{t,DNMP}}^{\text{cross-coupling}}$
Bridge DPNV	$\vec{v}_{t,term} = \vec{v}_{t,B} = \frac{L_t}{2}\frac{d}{dt}\vec{i}_{t,B} + \frac{R}{2}\vec{i}_{t,B} + \vec{e}_m$	$\vec{v}_{s,term} = \vec{v}_{s,B} = \frac{L_s}{2}\frac{d}{dt}\vec{i}_{s,B} + \frac{R}{2}\vec{i}_{s,B}$
Parallel DPNV	$\vec{v}_{t,term} = \overbrace{\frac{L_t}{2}\frac{d}{dt}\vec{i}_{t,P} + \frac{R}{2}\vec{i}_{t,P} + \vec{e}_m}^{\vec{v}_{t,P}} + \overbrace{R\vec{i}_{s,P} + L_s \frac{d}{dt}\vec{i}_{s,P}}^{\text{cross-coupling}}$	$\vec{v}_{s,term} = \vec{v}_{s,P} = 2L_s \frac{d}{dt}\vec{i}_{s,P} + 2R\vec{i}_{s,P}$
MCI	$\vec{v}_{t,term} = \vec{v}_{t,MCI} = 2L_t \frac{d}{dt}\vec{i}_{t,MCI} + 2R\vec{i}_{t,MCI} + 2\vec{e}_m$	$\vec{v}_{s,term} = \overbrace{\frac{L_s}{2}\frac{d}{dt}\vec{i}_{s,MCI} + \frac{R}{2}\vec{i}_{s,MCI} + \vec{e}_m}^{\vec{v}_{s,MCI}} + \overbrace{R\vec{i}_{t,MCI} + L_t \frac{d}{dt}\vec{i}_{t,MCI}}^{\text{cross-coupling}}$

3.2. ProposedUniversal Bearingless Motor Model

This paper proposes the generalized bearingless motor model shown in Figure 4. This model is developed from the perspective of Section 2 (MP winding), which provides the fundamental information of the machine. When the winding is connected to drive electronics in a different configuration (i.e., DNMP, bridge DPNV, parallel DPNV, and MCI), the terminal voltages and currents are transformed into the phase voltages and

currents of the MP winding model. The MP governing equations for shaft force/torque (Section 2.2) and voltage/current (Section 2.3) are used to model the machine's behavior, and then the resulting currents are transformed back into the resulting terminal currents.

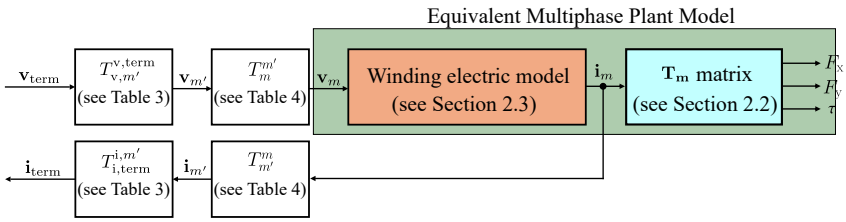


Figure 4. Proposed universal bearingless motor model; see Tables 3 and 4 for details of the transformation matrix blocks.

The proposed model (Figure 4) is now described in detail. The model input $\mathbf{v}_{\text{term}}$ is the voltage applied at the terminals of the motor relative to its neutral point. For Figure 3a, $\mathbf{v}_{\text{term}} = \mathbf{v}_m$, and for Figure 3b–e, $\mathbf{v}_{\text{term}} = [v_{u1}, v_{v1}, v_{w1}, v_{u2}, v_{v2}, v_{w2}]^\top$. This is converted to the coil group voltage $\mathbf{v}_{m'} = [v_{ua}, v_{ub}, v_{va}, v_{vb}, v_{wa}, v_{wb}]^\top$ using the transformation matrix $T^{\text{v,term}}_{\text{v},m'}$ presented in Table 4. Note that in this paper's nomenclature, $T^{\text{v,term}}_{\text{v},m'} = \left(T^{\text{v},m'}_{\text{v,term}}\right)^{-1}$, and $T^{\text{v},m'}_{\text{v,term}}$ is equivalent to the matrix $T^{\text{v},m}_{\text{v,ph}}$ introduced in [36] (Section V). Next, $\mathbf{v}_{m'}$ is converted to the voltage across each phase of the MP winding $\mathbf{v}_m$ through the matrix $T^{m'}_{m}$ of Table 5. This matrix depends on the number of pole-pairs p, p_s obtained through Equation (2) and implements the mapping summarized in [18,36] (Table I).

The MP phase voltage $\mathbf{v}_m$ is applied to the winding electric model (Section 2.3) to determine the MP phase current $\mathbf{i}_m$. The $\mathbf{T}_\text{m}$ matrix of Section 2.2 is multiplied by the phase currents to determine the shaft force and torque.

The MP phase currents $\mathbf{i}_m$ are converted to coil group currents $\mathbf{i}_{m'} = [i_{ua}, i_{ub}, i_{va}, i_{vb}, i_{wa}, i_{wb}]^\text{T}$ by $T^{m}_{m'}$ provided in Table 5. Here, positive currents enter the dotted terminals of Figure 3. The coil group currents are then converted to terminal currents $\mathbf{i}_{\text{term}}$ using $T^{\text{i},m'}_{\text{i,term}}$, where for Figure 3a, $\mathbf{i}_{\text{term}} = \mathbf{i}_m$, and for Figure 3b–e, $\mathbf{i}_{\text{term}} = [I_{u1}, I_{v1}, I_{w1}, I_{u2}, I_{v2}, I_{w2}]^\top$, with current defined as positive entering the motor. While the bridge DPNV winding still consists of six terminals as shown in Figure 3c, each phase of this winding configuration includes four coil groups (*a*–*d*) instead of two (*a*–*b*). As a result, the transformation matrices for bridge DPNV in Table 4 have 12 columns. The paper considers that coil groups *a* and *b*, and coil groups *c* and *d*, of the bridge DPNV configuration are created by splitting coil groups *a* and *b* of other combined windings in half. From this, the inverses of $T^{\text{v},m'}_{\text{v,term}}$ and $T^{\text{i},m'}_{\text{i,term}}$ are calculated by assuming that the voltage of coil groups *a* and *c*, and coil groups *b* and *d*, are equal in each phase (e.g., $v_{ua} = v_{uc}$ and $v_{ub} = v_{ud}$), and that the torque and suspension terminal currents are split equally between the two parallel paths.

Table 4. Voltage and current coil-group-to-terminal transformation matrices.

	DNMP	Bridge DPNV	Parallel DPNV	MCI
$T^{\text{v},m'}_{\text{v,term}}$	$\begin{bmatrix} 1 & 0 & 0 & 0 & 0 & 0 \\ 0 & 0 & 1 & 0 & 0 & 0 \\ 0 & 0 & 0 & 0 & 1 & 0 \\ 0 & 1 & 0 & 0 & 0 & 0 \\ 0 & 0 & 0 & 1 & 0 & 0 \\ 0 & 0 & 0 & 0 & 0 & 1 \end{bmatrix}$	$\begin{bmatrix} 1 & 0 & 0 & 1 & 0 & 0 & 0 & 0 & 0 & 0 & 0 & 0 \\ 0 & 0 & 0 & 0 & 1 & 0 & 0 & 1 & 0 & 0 & 0 & 0 \\ 0 & 0 & 0 & 0 & 0 & 0 & 0 & 0 & 1 & 0 & 0 & 1 \\ 0 & 0 & -1 & 1 & 0 & 0 & 0 & 0 & 0 & 0 & 0 & 0 \\ 0 & 0 & 0 & 0 & 0 & 0 & -1 & 1 & 0 & 0 & 0 & 0 \\ 0 & 0 & 0 & 0 & 0 & 0 & 0 & 0 & 0 & 0 & -1 & 1 \end{bmatrix}$	$\begin{bmatrix} 0 & 1 & 0 & 0 & 0 & 0 \\ 0 & 0 & 0 & 1 & 0 & 0 \\ 0 & 0 & 0 & 0 & 0 & 1 \\ -1 & 1 & 0 & 0 & 0 & 0 \\ 0 & 0 & -1 & 1 & 0 & 0 \\ 0 & 0 & 0 & 0 & -1 & 1 \end{bmatrix}$	$\begin{bmatrix} 1 & 1 & 0 & 0 & 0 & 0 \\ 0 & 0 & 1 & 1 & 0 & 0 \\ 0 & 0 & 0 & 0 & 1 & 1 \\ 0 & 1 & 0 & 0 & 0 & 0 \\ 0 & 0 & 0 & 1 & 0 & 0 \\ 0 & 0 & 0 & 0 & 0 & 1 \end{bmatrix}$
$T^{\text{i},m'}_{\text{i,term}}$	$\begin{bmatrix} 1 & 0 & 0 & 0 & 0 & 0 \\ 0 & 0 & 1 & 0 & 0 & 0 \\ 0 & 0 & 0 & 0 & 1 & 0 \\ 0 & 1 & 0 & 0 & 0 & 0 \\ 0 & 0 & 0 & 1 & 0 & 0 \\ 0 & 0 & 0 & 0 & 0 & 1 \end{bmatrix}$	$\begin{bmatrix} 1 & 1 & 0 & 0 & 0 & 0 & 0 & 0 & 0 & 0 & 0 & 0 \\ 0 & 0 & 0 & 0 & 1 & 1 & 0 & 0 & 0 & 0 & 0 & 0 \\ 0 & 0 & 0 & 0 & 0 & 0 & 0 & 0 & 1 & 1 & 0 & 0 \\ -1 & 0 & 0 & 1 & 0 & 0 & 0 & 0 & 0 & 0 & 0 & 0 \\ 0 & 0 & 0 & 0 & -1 & 0 & 0 & 1 & 0 & 0 & 0 & 0 \\ 0 & 0 & 0 & 0 & 0 & 0 & 0 & 0 & -1 & 0 & 0 & 1 \end{bmatrix}$	$\begin{bmatrix} 1 & 1 & 0 & 0 & 0 & 0 \\ 0 & 0 & 1 & 1 & 0 & 0 \\ 0 & 0 & 0 & 0 & 1 & 1 \\ -1 & 0 & 0 & 0 & 0 & 0 \\ 0 & 0 & -1 & 0 & 0 & 0 \\ 0 & 0 & 0 & -1 & 0 & 0 \end{bmatrix}$	$\begin{bmatrix} 1 & 0 & 0 & 0 & 0 & 0 \\ 0 & 0 & 1 & 0 & 0 & 0 \\ 0 & 0 & 0 & 0 & 1 & 0 \\ -1 & 1 & 0 & 0 & 0 & 0 \\ 0 & 0 & -1 & 1 & 0 & 0 \\ 0 & 0 & 0 & 0 & -1 & 1 \end{bmatrix}$

Table 5. Mapping matrices from 6-phase MP to DNMP, Parallel DPNV, and MCI coil groups ($T^{m}_{m'}$).

	Case 1 $\alpha_t = +\pi/3$ $\alpha_s = +2\pi/3$	**Case 2** $\alpha_t = +2\pi/3$ $\alpha_s = +\pi/3$	**Case 3** $\alpha_t = -\pi/3$ $\alpha_s = -2\pi/3$	**Case 4** $\alpha_t = -2\pi/3$ $\alpha_s = -\pi/3$
$[u_a, u_b, v_a, v_b, w_a, w_b]$	$[-4, +1, -6, +3, -2, +5]$	$[+4, +1, +2, +5, +6, +3]$	$[-4, +1, -2, +5, -6, +3]$	$[+4, +1, +6, +3, +2, +5]$
$T^{m}_{m'}$	$\begin{bmatrix} 0 & 0 & 0 & -1 & 0 & 0 \\ 1 & 0 & 0 & 0 & 0 & 0 \\ 0 & 0 & 0 & 0 & 0 & -1 \\ 0 & 0 & 1 & 0 & 0 & 0 \\ 0 & -1 & 0 & 0 & 0 & 0 \\ 0 & 0 & 0 & 0 & 1 & 0 \end{bmatrix}$	$\begin{bmatrix} 0 & 0 & 0 & 1 & 0 & 0 \\ 1 & 0 & 0 & 0 & 0 & 0 \\ 0 & 1 & 0 & 0 & 0 & 0 \\ 0 & 0 & 0 & 0 & 1 & 0 \\ 0 & 0 & 0 & 0 & 0 & 1 \\ 0 & 0 & 1 & 0 & 0 & 0 \end{bmatrix}$	$\begin{bmatrix} 0 & 0 & 0 & -1 & 0 & 0 \\ 1 & 0 & 0 & 0 & 0 & 0 \\ 0 & -1 & 0 & 0 & 0 & 0 \\ 0 & 0 & 0 & 0 & 1 & 0 \\ 0 & 0 & 0 & 0 & 0 & -1 \\ 0 & 0 & 1 & 0 & 0 & 0 \end{bmatrix}$	$\begin{bmatrix} 0 & 0 & 0 & 1 & 0 & 0 \\ 1 & 0 & 0 & 0 & 0 & 0 \\ 0 & 0 & 0 & 0 & 0 & 1 \\ 0 & 0 & 1 & 0 & 0 & 0 \\ 0 & 1 & 0 & 0 & 0 & 0 \\ 0 & 0 & 0 & 0 & 1 & 0 \end{bmatrix}$

4. Universal Force and Torque Controller

This section introduces a force/torque controller applicable to bearingless motors with any winding configuration and combination of p and p_s, shown in Figure 5. The controller is implemented using an analogous approach to the model of Section 3.2: the controller acts on the MP electric model (Section 2.4) by transforming terminal currents/voltages of each specific winding into MP currents/voltages.

In Figure 5, the "Generate Current References" block converts torque $\vec{T}^{\text{ref}}$ and force $\vec{F}^{\text{ref}}$ commands into current references. Figure 6 illustrates two implementations: (1) a space vector calculation (Figure 6a) obtained by solving Equation (11) and (2) a more general matrix-based approach (Figure 6b), [38,39]. The matrix approach does not require sinusoidal entries in the $\mathbf{T}_m$ matrix and is suited for bearingless motor systems with higher-order force and torque harmonics. Note that in Figure 6a, $\vec{F}^{\text{ref}}$ should be replaced by $\vec{F}^{\text{ref}*}$ for $p_s = p - 1$ machines (see Equation (11)).

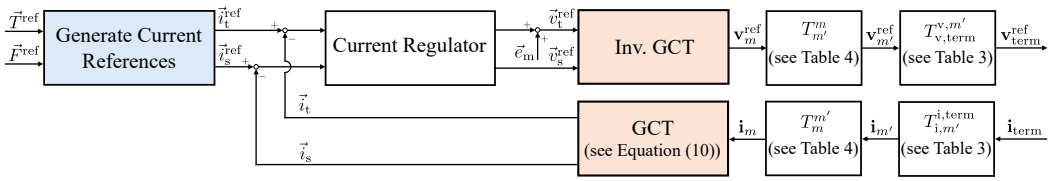
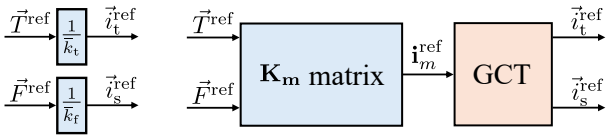


Figure 5. Proposed universal force and torque controller; see Figure 6 for details of the "Generate Current References" block.



(**a**) (**b**)

Figure 6. Generation of current references based on force/torque commands: (**a**) space vector approach, (**b**) $\mathbf{K}_m$ matrix approach.

In the "Current Regulator" block, well-known control strategies can be used, such as vector PI control or complex vector current regulation, implemented either in the stationary or synchronous frame, as discussed in [37]. Regardless of the specific current regulator or winding configurations, the proposed controller always sees the plant of the MP winding in Equation (12). This allows the current regulator to be tuned using only L_t, L_s, and R. The cross-coupling voltages between torque and suspension terminals observed in DNMP, parallel DPNV, and MCI windings (see Table 3) are handled automatically via the transformation matrices of Tables 4 and 5 as a feedforward compensation.

In summary, the proposed generalized controller allows a bearingless motor with any combined-winding type to be designed for the plant model of the multiphase winding

configuration. This illustrates the equivalence of these machines and provides a starting point for winding-specific controller development.

5. Simulink Model

This section presents the implementation of the generalized bearingless motor model (Figure 4) and controller (Figure 5) in Simulink. The resulting model files are published publicly in the authors' GitHub repository, available at https://github.com/severson-group/bm-modeling (accessed on 22 May 2026). This repository includes a README file that provides detailed instructions on the required MATLAB/Simulink version and explains how to use the provided scripts to reproduce the results presented in this section.

The Simulink model enables simulations based on user-specified winding configurations and motor parameters. A MATLAB setup script is provided where users indicate the winding type and the parameters of Equations (11) and (12). The Simulink files automatically apply the corresponding transformations and controller tuning. The current regulators are implemented as synchronous-frame PI controllers. The files are developed in a modular fashion, so that users can replace components and adapt them to meet the specifics of their machine and control environment (for example, replacing the generalized controller with a controller specific to their winding type, or replacing the generalized model with a motor/winding-specific model).

To demonstrate the proposed universal bearingless motor model, a case-study bearingless machine with $p = 7$ and $p_s = 8$ is now introduced. The parameters of the case-study machine are summarized in Table 6, and the machine is evaluated with its winding connected in the forms DNMP, bridge DPNV, parallel DPNV, and MCI. Example simulation results are presented in Figure 7. In this simulation, step torque and force commands are issued (first two rows) while the shaft is spinning at 100 RPM.

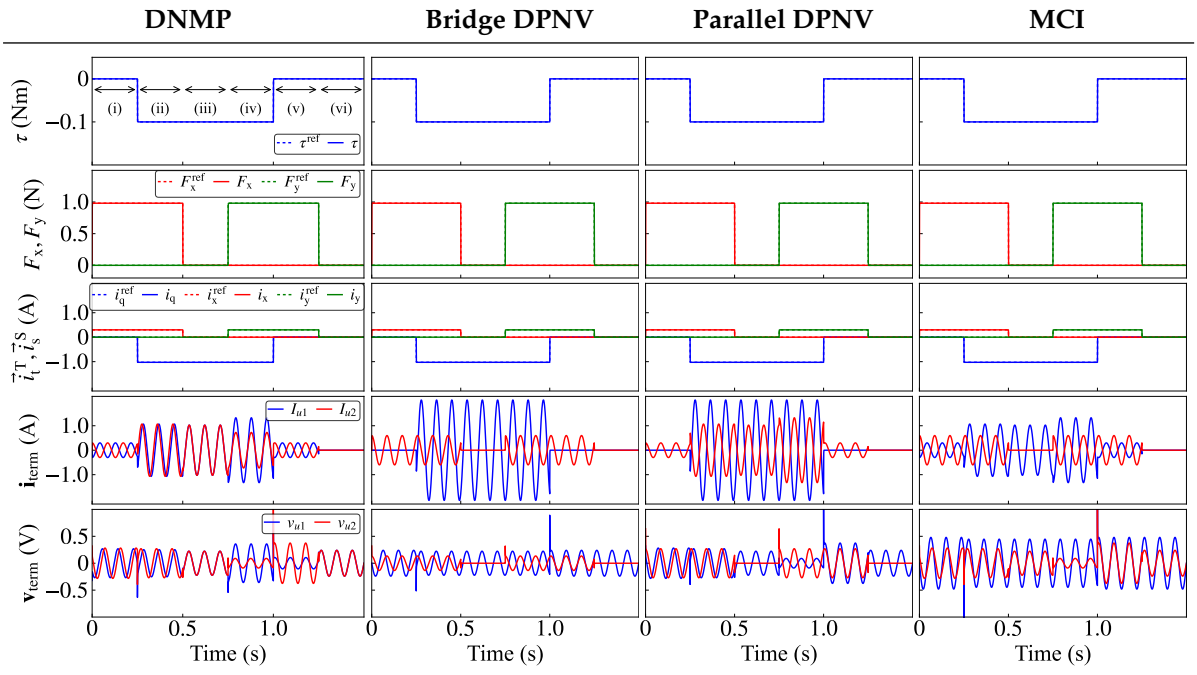


Figure 7. Simulink simulation results using the proposed universal controller and model, with the model parameters listed in Table 6; (i) only F_x^{ref} is issued, (ii) both τ^{ref} and F_x^{ref} are issued, (iii) only τ^{ref} is issued, (iv) both τ^{ref} and F_y^{ref} are issued, (v) only F_y^{ref} is issued, and (vi) all force and torque currents are zero.

Table 6. Model parameters.

Parameter	Value
p	7
p_s	8
L_t	0.38 mH
L_s	0.33 mH
R	0.45 Ω
k_e	22.9 mV/(rad/s)
k_t	0.097 Nm/A
k_f	3.3 N/A

The third row shows the torque and suspension currents of Equation (11) in the synchronous frame. As expected, these currents are identical across all winding configurations, demonstrating that the proposed generalized model treats all currents as the equivalent multiphase winding model. In contrast, the fourth row shows the terminal currents in phase U, which differ for each winding configuration. For example, in region (i), where only F_x^{ref} is issued, the bridge DPNV and parallel DPNV windings contain only suspension currents, whereas the multiphase and MCI windings contain both torque and suspension currents. This is especially evident in the MCI configuration, where half of the suspension current appears on the torque terminals. Similarly, in region (iii), where only τ^{ref} is generated, half of the torque current appears on the suspension terminals in the parallel DPNV winding.

The fifth row shows the terminal voltage in phase U. Again, notable differences can be observed for each winding type. This is best illustrated in region (vi), where although all force and torque currents are zero, back-EMF is induced at the torque terminals of all windings; however, for the bridge DPNV and parallel DPNV windings, no back-EMF appears on the suspension terminals, clearly demonstrating the DPNV property of these windings.

In summary, the proposed universal model/controller enables all combined windings to be treated within the equivalent multiphase winding model through transformation matrices and to use a single set of controller tuning parameters. This is verified through Simulink simulations and shown to yield equivalent step force and torque results for all windings.

6. Experimental Validation

This section presents the validation results of the proposed universal modeling and control framework using a prototype of the case-study bearingless machine described in Section 5. The following subsections describe the experimental setup, controller implementation with the universal model, and experimental results comparing the terminal current behaviors with DNMP, parallel DPNV, and MCI configurations.

6.1. Experimental Setup

Figure 8 shows the fabricated case-study machine introduced in Section 5. This case-study machine consists of a 12-slot stator with concentrated windings, where all terminal connections are accessible through the terminal blocks, enabling it to be configured into MP, DNMP, parallel DPNV, and MCI topologies. Detailed specifications of the case-study machine are provided in Table 7.

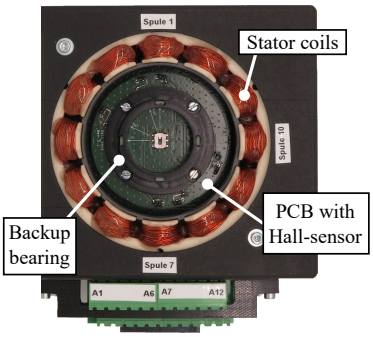


Figure 8. The case-study machine without the rotor, showing the radial backup bearing and a PCB mounted with Hall-sensors for rotor angle measurement.

Table 7. Specifications of the case-study machine.

Parameter	Value
Mechanical radial airgap length	2 mm
Stack length	10 mm
Rotor outer diameter	67 mm
Stator outer diameter	100 mm
Shaft diameter	42 mm
Shaft length	43.4 mm
PM material	NdFeB N40
Core material	M400-50A
Coil diameter	0.5 mm
Rated coil current	1 A_{rms}

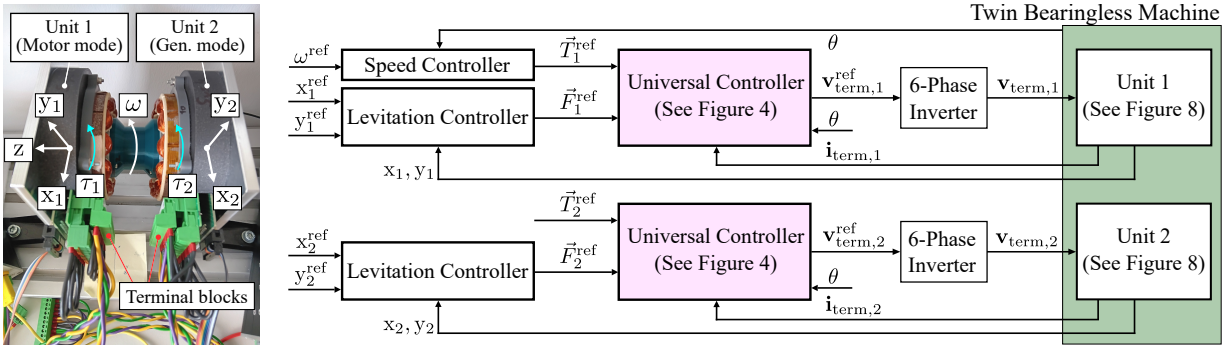
Figure 9a shows the experimental setup along with the definition of the coordinate system. In this setup, the rotors of two identical case-study machines are mechanically coupled along the z-axis through a shared shaft to form a twin bearingless machine configuration. Here, the left machine is defined as Unit 1 (denoted by a subscript 1), while the right machine is defined as Unit 2 (subscript 2). This twin configuration independently controls the radial positions and torque for each unit. Since each unit generates its own torque and force references based on rotor position measurements, no synchronization of commands between the two units is required. This allows full levitation testing to be achieved while applying load torque by operating Unit 1 under speed control (motor operation) and Unit 2 under torque control (generator operation). The axial degree of freedom is passively stabilized by the reluctance forces generated by the rotor magnets. The backup bearings allow the shaft to move by approximately ± 1 mm along the z-axis.

Figure 9b illustrates the control block diagram, including the proposed universal controller. For Unit 1, the control system includes both speed and levitation controllers. In contrast, Unit 2 employs only the levitation controller, while the torque command $\vec{T}_2^{\text{ref}}$ is directly applied to generate load torque. Conventional PID controllers are used in both the levitation controller [40–43] and the speed controller [44]. These controllers output the torque and force references used by the proposed universal controller. The sampling frequency of the current regulator and motion controllers is 20 kHz. In the universal controller, the mapping matrix for Case 1 (see Table 5) is used, since the case-study machine is configured with $p = 7$ and $p_s = 8$ (see Table 6). The controller gains used in this experiment are summarized in Table 8.

Table 8. Controller parameters used in the experiment.

Parameter	Value
Current regulator P gain	1
Speed controller P gain	0.8
Speed controller I gain	0.4
Levitation controller P gain	2.1
Levitation controller I gain	11
Levitation controller D gain	0.006

The Universal Controller outputs a commanded terminal voltage of $\mathbf{v}_{\text{term}}^{\text{ref}}$ that is provided to the "6-Phase Inverter" block to generate the actual terminal voltages $\mathbf{v}_{\text{term}}$. These inverter blocks are implemented in hardware using two standard three-phase inverters [45], providing a total of six phase legs for each unit. The inverters operate with a switching frequency of 20 kHz and a dead time of 200 ns. Based on this power electronics setup, experimental validation can be achieved for the DNMP, parallel DPNV, and MCI configurations. For the bridge DPNV, a different power electronics hardware is required, such as three full-bridge inverters, each powered by an isolated DC bus, and therefore, its experimental validation is not included in this paper. The inverters feature shunt resistors and integrated amplifiers for measuring the terminal currents ($\mathbf{i}_{\text{term},1}$ and $\mathbf{i}_{\text{term},2}$). Radial displacement signals (x_1, y_1, x_2, and y_2) are measured using eddy current sensors. The rotor angle θ is obtained using Hall-effect sensors mounted on the PCB (see Figure 8). A rotor angle compensation factor of 7.33×10^{-5} (rad/RPM) is applied to compensate for angle sensor signal delays. While each unit employs its own set of sensors, all measured signals are processed by a single CPU controller. Note that this experimental setup does not include dedicated torque or force sensors. However, the torque and radial forces can be computed from the measured terminal currents using the machine constants summarized in Table 6.



(**a**) (**b**)

Figure 9. Experimental setup: (**a**) the case-study machine configured as a twin bearingless machine; (**b**) a block diagram to demonstrate the proposed universal controller.

6.2. Experimental Scenarios

To experimentally validate the operating conditions presented in Figure 7, two scenarios are demonstrated while the rotor is levitated and rotated at 100 RPM, as follows:

(1) Apply a step torque of -0.1 Nm to Unit 2 to generate a load torque on the shaft while maintaining zero force commands. This scenario corresponds to region (iii) in Figure 7;

(2) Step suspension force while applying no load torque. This scenario corresponds to the operating condition shown in region (v) of Figure 7.

In these experiments, Unit 2's terminal connections are modified to realize DNMP, parallel DPNV, or MCI configurations, while Unit 1 remains configured as an MP winding. All measurement data presented in the following section are obtained from Unit 2.

These two experimental scenarios can be achieved by intentionally changing the shaft position of the twin bearingless machine, as illustrated in Figure 10. The left side of Figure 10 depicts the shaft located at its geometric center. Assuming a shaft mass of m, each unit experiences a gravimetric load of $mg/2$. Therefore, suspension forces of $F_{y,1} = F_{y,2} = mg/2$ are required for each unit to levitate the shaft. The middle of the cross-section in Figure 10 corresponds to experimental scenario 1. By issuing a positive position offset (see green dashed line), the unbalanced magnetic pull force (F_{UMP}) generated by each unit balances the gravitational load, i.e., $F_{UMP} = mg/2$. As a result, no suspension force is required and only load torque τ_2 can be applied. These positions with zero suspension force are determined experimentally by adjusting the position references until the suspension current commands become zero. The resulting shaft positions are then defined as $y_1 = y_2 = 0$ in this paper. In contrast, the right side of Figure 10 corresponds to experimental scenario 2. Here, the shaft position of Unit 1 remains $y_1 = 0$, while the position of Unit 2 is displaced to $y_2 = -0.3$ mm. Consequently, the suspension force of $F_{y,2} = mg/2 - F_{UMP} > 0$ must be generated to maintain levitation, thereby producing nonzero suspension forces while the torque command is zero.

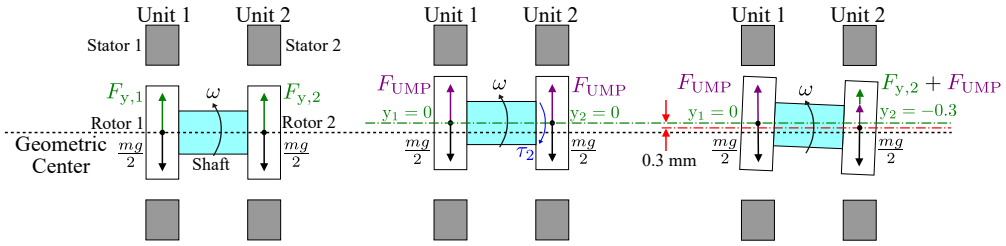


Figure 10. Cross-section of the shaft position along the y-axis. (**Left**) The shaft is located at its geometric center, requiring suspension force $F_{y,1}$ and $F_{y,2}$ to compensate for gravity. (**Middle**) The shaft is located at the position where UMP and gravitational force are balanced (this position is defined as $y_1 = y_2 = 0$). (**Right**) The shaft is displaced to $y_1 = 0$ and $y_2 = -0.3$ mm, requiring a suspension force of $F_{y,2} > 0$.

6.3. Experimental Results

This section presents the experimental results. Figure 11a shows the experimental results for scenario 1 with DNMP, parallel DPNV, and MCI configurations. At $t = 0$ ms, the machine is levitated and operated at a constant rotational speed of 100 RPM. Under this condition, the y-axis suspension force reference $F_{y,2}^{ref}$ remains zero since $F_{UMP} = mg/2$. At $t = 50$ ms, a negative torque command of -0.1 Nm is applied to Unit 2. In this case, the force reference is still zero, as observed in the third row in Figure 11a. Since this scenario produces only torque currents, the measured terminal currents can be directly compared with region (iii) in Figure 7. As expected, for the DNMP configuration, the torque and suspension currents almost match, whereas in the parallel DPNV configuration, these currents oppose one another. In the parallel DPNV configuration, half of the torque current appears at the suspension terminals, in agreement with the simulation results. For MCI, a small suspension current of approximately 0.5 A is observed before the torque step is applied. This suspension current remains unchanged after the torque step is applied, demonstrating that the torque step does not influence the suspension current, as expected for the MCI configuration.

Figure 11b shows the experimental results for scenario 2 with DNMP, parallel DPNV, and MCI configurations. At $t = 50$ ms, a position reference offset of -0.3 mm is applied in the negative y_2 direction to Unit 2. In this condition, F_{UMP} decreases, and this reduction is

compensated by the levitation controller by issuing a positive suspension force command of approximately $F_{y,2}^{ref} = 1$ N, as shown in the third row of Figure 11b. The DNMP and MCI configurations have torque and suspension currents that are approximately opposite in polarity. In the parallel DPNV configuration, the torque terminal current remains nearly zero, and only the suspension current is observed as expected. Again, these measurements are consistent with the simulation results.

In summary, all results were obtained by controlling the prototype machine with the proposed universal controller concept (Figure 5) and mapping matrices (Tables 4 and 5). The results show strong agreement with the simulations of Section 5 and therefore validate the proposed universal controller concept for DNMP, parallel DPNV, and MCI configurations.

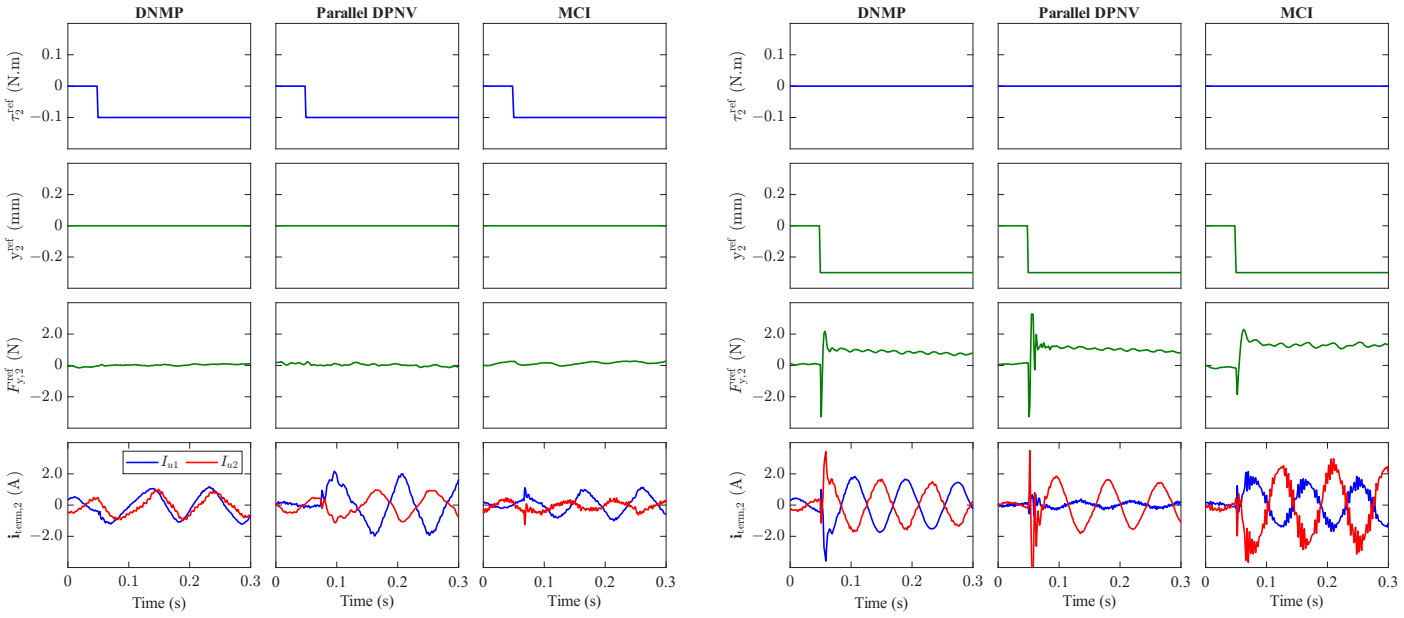


Figure 11. Experimental results of DNMP, parallel DPNV, and MCI: (**a**) torque step response τ_2^{ref}, corresponding to region (iii) in Figure 7, and (**b**) y step response, corresponding to the operating condition shown in region (v) of Figure 7.

7. Conclusions

This paper presents a generalized simulation model for radial flux non-salient bearingless motors that accommodates all types of combined-winding configurations with six phases, aiming to support ongoing and future research in this domain. The model and controller are developed based on calculating the phase voltage and current of the winding, when it is viewed as a multiphase winding, from the terminal voltages and currents of any combined-winding configuration. The paper finds that this allows for the creation of (1) a universal model of the force/torque and voltage/current behavior of the machine and (2) a universal control implementation where the same current regulator can be applied to any combined-winding bearingless motor without needing to re-tune the controller gains when switching between winding types.

Note that the universal controller is unlikely to be used as the final control implementation of a bearingless motor. This is especially true in bridge DPNV, parallel DPNV, and MCI combined windings, where the goal of using these windings is typically to enable the use of separate motor and suspension inverters and controllers, and therefore, a single combined motor/force controller is not viable. Instead, the proposed universal controller/model provides a trusted starting point for control development and simulation. As a user's control architecture matures, they are expected to progressively replace

"universal" components with architecture-specific components (for example, in a bridge DPNV, first changing the universal controller to separate torque and force controllers, then replacing the model with a true 12-coil-group machine, and then introducing single- and three-phase inverters, and so on, until the simulation environment fully reflects the user's hardware). Similarly, more accurate modeling approaches may be required to account for rotor saliency, magnetic saturation, slotting harmonics, rotor eccentricity, inverter nonidealities, and the nonlinear relationship between force, current, and rotor position. At each step, users can compare simulation results with the trusted universal controller/model to ensure proper functionality.

Author Contributions: Conceptualization, T.N., M.M., K.N.V.P. and E.L.S.; methodology, T.N., M.M., K.N.V.P., W.G. and E.L.S.; software, T.N., M.M., K.N.V.P. and W.G.; validation, T.N., M.M., D.P. and W.G.; formal analysis, T.N., M.M., W.G. and E.L.S.; investigation, T.N., M.M., K.N.V.P., D.P., W.G. and E.L.S.; resources, T.N., M.M., K.N.V.P., D.P., W.G. and E.L.S.; data curation, T.N., M.M., K.N.V.P., D.P.; writing—original draft preparation, T.N.; writing—review and editing, T.N., M.M., K.N.V.P., W.G. and E.L.S.; visualization, T.N. and M.M.; supervision, W.G. and E.L.S.; project administration, W.G. and E.L.S.; funding acquisition, W.G. and E.L.S. All authors have read and agreed to the published version of the manuscript.

Funding: Parts of this work were conducted within the COMET K2 Center for Symbiotic Mechatronics at the Linz Center of Mechatronics (LCM), funded by the Austrian and Upper Austrian governments.

Institutional Review Board Statement: Not applicable.

Informed Consent Statement: Not applicable.

Data Availability Statement: The original contributions presented in this study are included in the article.

Conflicts of Interest: Wolfgang Gruber receives public funding from the European Union (# 101112338), the Austrian Research Promotion Agency FFG (# 4106531) and Technology Agency of the Czech Republic TACR (# TS01030197). Wolfgang Gruber and Eric Severson are voluntarily and non-remunerated members of the International Advisory Committee of the International Symposium on Magnetic Bearings (ISMB). Wolfgang Gruber is an employee of Johannes Kepler University Linz (JKU), Austria. Wolfgang Gruber holds a patent on bearingless motors (WO2012162716A3). David Prinz is an employee of Linz Center of Competence in Mechatronics GmbH (LCM). Takahiro Noguchi, Mohamadhasan Mokhtarabadi, KNV Prasad, and Eric Severson are employees of the University of Minnesota. The authors declare no conflicts of interest.

Nomenclature

The following nomenclature is used in this manuscript:

Symbol	Description	Unit
α	Arbitrary angular location in the stator airgap	rad
α_{t}, α_{s}	Phase separation angle for torque and suspension winding	rad
$\alpha_{\mathrm{w0},p}$, $\alpha_{\mathrm{w0},p_{\mathrm{s}}}$	Winding function phase shift for torque and suspension winding	rad
γ	Angular position of the magnetic field produced by the winding	rad
δ	Length of the airgap	m
θ_{mech}	Mechanical angular position of the rotor	rad
θ	Electrical angular position of the rotor ($\theta = p\theta_{\mathrm{mech}}$)	rad
λ_k	Flux linkage of the k-th phase	Wb
μ_0	Permeability of free space	H/m
ω	Electrical angular velocity	rad/s
σ_{n}, σ_{tan}	Normal and tangential components of the Maxwell stress	Pa
τ	Electromagnetic shaft torque	Nm

$\hat{\tau}$	Peak torque per phase current	Nm/A
ϕ'_{t}, ϕ'_{s}	Phase angles of the torque and suspension current vectors	rad
$B_\delta(\alpha)$	Magnetizing radial airgap flux density	T
$\hat{B}_\delta$	Peak magnetizing radial airgap flux density	T
$B_{n,\mathrm{tan}}$	Tangential flux density of the n-th harmonic	T
B_w	Radial airgap flux density generated by winding currents	T
c	Coefficient of the generalized Clarke transformation	–
e_k	Back-electromotive force (EMF) of the k-th phase	V
F_{x}, F_{y}	Radial forces along the x- and y-axes	N
$F_{\mathrm{x},k}$, $F_{\mathrm{y},k}$	Radial force components produced by the k-th phase winding	N
$\hat{f}$	Peak radial force per phase current	N/A
$\hat{I}_{\mathrm{t}}$, $\hat{I}_{\mathrm{s}}$	Magnitudes of the torque and suspension current vectors	A
i_k	Instantaneous phase current of the k-th phase	A
i_{d}, i_{q}	d- and q-axis currents	A
i_{x}, i_{y}	x- and y-axis currents	A
k	Phase number ($k = 1, \ldots, m$)	–
k_{e}	Back-EMF constant	V/(rad/s)
k_{f}	Force constant	N/A
$\bar{k}_{\mathrm{f}}$	Force constant in the synchronous frame	N/A
k_{t}	Torque constant	Nm/A
$\bar{k}_{\mathrm{t}}$	Torque constant in the synchronous frame	Nm/A
l	Axial length of the rotor	m
$L_{j,k}$	Mutual inductance between phases j and k	H
L_0	Average phase inductance	H
L_{t}, L_{s}	Torque and suspension self-inductances	H
m	Number of phases, mass	kg
$N_k(\alpha)$	Idealized phase winding function of the k-th phase	Turns
$\hat{N}_n$	Amplitude of the n-th harmonic winding function	Turns
N_p, $N_{p_{\mathrm{s}}}$	Winding function amplitudes for torque and suspension fields	Turns
n	Harmonic order	–
p, p_{s}	Number of torque and suspension pole-pairs	–
r	Radius of the airgap	m
R	Phase resistance	Ω
T_{d}	Flux-weakening component	Nm
$\vec{F}$	Force space vector	N
$\vec{i}_{\mathrm{t}}$, $\vec{i}_{\mathrm{s}}$	Torque and suspension current space vectors	A
$\vec{i}_{\mathrm{t}}^{\mathrm{T}}$, $\vec{i}_{\mathrm{s}}^{\mathrm{S}}$	Torque and suspension current vectors in the synchronous frame	A
$\vec{T}$	Torque space vector	Nm
$\vec{v}_{\mathrm{t}}$, $\vec{v}_{\mathrm{s}}$	Torque and suspension voltage space vectors	V
$\mathbf{e}_m$	Back-EMF vector	V
$\mathbf{i}_m$	Multiphase current vector	A
$\mathbf{i}_{m'}$	Coil-group current vector	A
$\mathbf{i}_{\mathrm{term}}$	Terminal current vector	A
$\mathbf{L}$	Inductance matrix	H
$\mathbf{M}_{\mathrm{c}}$	Cogging force/torque matrix	–
$\mathbf{R}$	Resistance matrix	Ω
$\mathbf{T}_{\mathrm{m}}$	Force/torque mapping matrix	–
$T^{\mathrm{i},m'}_{\mathrm{i,term}}$	Current coil-group-to-terminal transformation matrix	–
$T^{m}_{m'}$	Mapping matrix	–
$T^{\mathrm{v},m'}_{\mathrm{v,term}}$	Voltage coil-group-to-terminal transformation matrix	–
$\mathbf{v}_m$	Multiphase voltage vector	V
$\mathbf{v}_{m'}$	Coil-group voltage vector	V
$\mathbf{v}_{\mathrm{term}}$	Terminal voltage vector	V

https://doi.org/10.3390/act15080410

References

1. Okada, Y.; Yamashiro, N.; Ohmori, K.; Masuzawa, T.; Yamane, T.; Konishi, Y.; Ueno, S. Mixed flow artificial heart pump with axial self-bearing motor. *IEEE/ASME Trans. Mechatron.* **2005**, *10*, 658–665. [CrossRef]
2. Bourque, K.; Gernes, D.B.; Loree, H.M.; Scott Richardson, J.; Poirier, V.L.; Barletta, N.; Fleischli, A.; Foiera, G.; Gempp, T.M.; Schoeb, R.; et al. HeartMate III: Pump design for a centrifugal LVAD with a magnetically levitated rotor. *ASAIO J.* **2001**, *47*, 401–405. [CrossRef] [PubMed]
3. Greatrex, N.A.; Timms, D.L.; Kurita, N.; Palmer, E.W.; Masuzawa, T. Axial magnetic bearing development for the BiVACOR rotary BiVAD/TAH. *IEEE Trans. Biomed. Eng.* **2009**, *57*, 714–721. [CrossRef] [PubMed]
4. Reichert, T.; Nussbaumer, T.; Kolar, J.W. Bearingless 300-W PMSM for bioreactor mixing. *IEEE Trans. Ind. Electron.* **2011**, *59*, 1376–1388. [CrossRef]
5. Warberger, B.; Kaelin, R.; Nussbaumer, T.; Kolar, J.W. 50-N·m/2500-W Bearingless Motor for High-Purity Pharmaceutical Mixing. *IEEE Trans. Ind. Electron.* **2011**, *59*, 2236–2247.
6. Reichert, T.; Nussbaumer, T.; Kolar, J.W. Investigation of exterior rotor bearingless motor topologies for high-quality mixing applications. *IEEE Trans. Ind. Appl.* **2012**, *48*, 2206–2216. [CrossRef]
7. Kascak, P.; Jansen, R.; Dever, T.; Nagorny, A.; Loparo, K. Levitation performance of two opposed permanent magnet pole-pair separated conical bearingless motors. In *Proceedings of the 2011 IEEE Energy Conversion Congress and Exposition*; IEEE: Piscataway, NJ, USA, 2011; pp. 1649–1656.
8. Ooshima, M.; Kobayashi, S.; Tanaka, H. Magnetic suspension performance of a bearingless motor/generator for flywheel energy storage systems. In *Proceedings of the IEEE PES General Meeting*; IEEE: Piscataway, NJ, USA, 2010; pp. 1–4.
9. Sun, X.; Su, B.; Wang, S.; Yang, Z.; Lei, G.; Zhu, J.; Guo, Y. Performance analysis of suspension force and torque in an IBPMSM with V-shaped PMs for flywheel batteries. *IEEE Trans. Magn.* **2018**, *54*, 8105504. [CrossRef]
10. Munteanu, G.; Binder, A.; Schneider, T. Loss measurement of a 40 kW high-speed bearingless PM synchronous motor. In *Proceedings of the 2011 IEEE ECCE*; IEEE: Piscataway, NJ, USA, 2011; pp. 722–729. [CrossRef]
11. Jastrzebski, R.P.; Jaatinen, P.; Sugimoto, H.; Pyrhönen, O.; Chiba, A. Design of a bearingless 100 kW electric motor for high-speed applications. In *Proceedings of the 2015 18th International Conference on Electrical Machines and Systems (ICEMS)*; IEEE: Piscataway, NJ, USA, 2015; pp. 2008–2014. [CrossRef]
12. Liu, Z.; Chiba, A.; Irino, Y.; Nakazawa, Y. Optimum Pole Number Combination of a Buried Permanent Magnet Bearingless Motor and Test Results at an Output of 60 kW With a Speed of 37000 r/min. *IEEE Open J. Ind. Appl.* **2020**, *1*, 33–41. [CrossRef]
13. Schneider, T.; Petersen, J.; Binder, A. Influence of pole pair combinations on high-speed bearingless permanent magnet motor. In *Proceedings of the 4th IET International Conference on Power Electronics, Machines and Drives (PEMD 2008)*; IET: London, UK, 2008; pp. 707–711.
14. Bergmann, G.; Binder, A. Design guidelines of bearingless PMSM with two separate poly-phase windings. In *Proceedings of the 2016 XXII International Conference on Electrical Machines (ICEM)*; IEEE: Piscataway, NJ, USA, 2016; pp. 2588–2594. [CrossRef]
15. Dietz, D.; Binder, A. Eddy current influence on the control behavior of bearingless PM synchronous machines. *IEEE Trans. Ind. Appl.* **2021**, *57*, 6944–6955. [CrossRef]
16. Sun, X.; Chen, L.; Yang, Z. Overview of Bearingless Permanent-Magnet Synchronous Motors. *IEEE Trans. Ind. Electron.* **2013**, *60*, 5528–5538. [CrossRef]
17. Ramadas, B.; Severson, E.L. Rethinking the Design of Non-Salient Bearingless Permanent Magnet Machines. *IEEE Trans. Ind. Appl.* **2023**, *59*, 3368–3380. [CrossRef]
18. Khamitov, A.; Petersen, N.P.; Severson, E.L. Combined windings for bearingless motors—An overview. In *Proceedings of the 2023 IEEE Energy Conversion Congress and Exposition (ECCE)*; IEEE: Piscataway, NJ, USA, 2023; pp. 4628–4635.
19. Khamitov, A.; Severson, E.L. Design of multi-phase combined windings for bearingless machines. *IEEE Trans. Ind. Appl.* **2023**, *59*, 3243–3255. [CrossRef]
20. Gruber, W.; Silber, S. Dual field-oriented control of bearingless motors with combined winding system. In *Proceedings of the 2018 International Power Electronics Conference (IPEC-Niigata 2018-ECCE Asia)*; IEEE: Piscataway, NJ, USA, 2018; pp. 4028–4033.
21. Milan, H.; Ojeda, J.; Wang, M.; Carbone, L.; Degano, M.; Gerada, C.; Di Nardo, M.; Cizeron, A. An Online Analytical Solution for Multi-Sector Bearingless Machine Current Reference Calculation. In *Proceedings of the 2025 Energy Conversion Congress & Expo Europe (ECCE Europe)*; IEEE: Piscataway, NJ, USA, 2025; pp. 1–5.
22. Dietz, D.; Binder, A. Comparison between a bearingless pm motor with separated and combined winding for torque and lateral force generation. In *Proceedings of the 2019 21st European Conference on Power Electronics and Applications (EPE'19 ECCE Europe)*; IEEE: Piscataway, NJ, USA, 2019; pp. P.1–P.10.
23. Raggl, K.; Nussbaumer, T.; Kolar, J.W. Comparison of separated and combined winding concepts for bearingless centrifugal pumps. *J. Power Electron.* **2009**, *9*, 243–258.
24. Silber, S.; Amrhein, W.; Bosch, P.; Schob, R.; Barletta, N. Design aspects of bearingless slice motors. *IEEE/ASME Trans. Mechatron.* **2005**, *10*, 611–617. [CrossRef]

25. Reichert, T.; Kolar, J.W.; Nussbaumer, T. Design study for exterior rotor bearingless permanent magnet machines. In *Proceedings of the 2011 IEEE Energy Conversion Congress and Exposition*; IEEE: Piscataway, NJ, USA, 2011; pp. 3377–3382. [CrossRef]
26. Mitterhofer, H.; Mrak, B.; Gruber, W. Comparison of high-speed bearingless drive topologies with combined windings. *IEEE Trans. Ind. Appl.* **2014**, *51*, 2116–2122. [CrossRef]
27. Wen, Z.; Valente, G.; Formentini, A.; Papini, L.; Gerada, C.; Zanchetta, P. Open-Circuit Fault Control Techniques for Bearingless Multisector Permanent Magnet Synchronous Machines. *IEEE Trans. Ind. Appl.* **2021**, *57*, 2527–2536. [CrossRef]
28. Mokhtarabadi, M.; Prasad, K.N.; Noguchi, T.; Severson, E.L. Sizing of the Suspension Converter Power Electronics for Bearingless Motors. In *Proceedings of the 2025 IEEE Energy Conversion Conference Congress and Exposition (ECCE)*; IEEE: Piscataway, NJ, USA, 2025; pp. 1–8.
29. Noguchi, T.; Mokhtarabadi, M.; Prasad, K.; Gruber, W.; Severson, E. Model and Control Framework for Bearingless Motors with Combined Windings. In *Proceedings of the 19th International Symposium on Magnetic Bearings, ISMB*; Oxford University Press: Oxford, UK, 2025; pp. 1–8.
30. Lipo, T.A. *Analysis of Synchronous Machines*; CRC Press: Boca Raton, FL, USA, 2017.
31. Sung, D.; Noguchi, T.; Kang, S.G.; Severson, E. System Identification and Sensor Calibration Methods for Commissioning of Bearingless Machines. In *Proceedings of the 19th International Symposium on Magnetic Bearings, ISMB*; Oxford University Press: Oxford, UK, 2025; pp. 1–8.
32. Khoo, W.; Fittro, R.L.; Garvey, S.D. AC polyphase self-bearing motors with a bridge configured winding. In *Proceedings of the 7th International Symposium on Magnetic Bearings*; ETH Zurich: Zürich, Switzerland, 2002; pp. 47–52.
33. Khoo, W.; Kalita, K.; Garvey, S. Practical implementation of the bridge configured winding for producing controllable transverse forces in electrical machines. *IEEE Trans. Magn.* **2011**, *47*, 1712–1718. [CrossRef]
34. Oishi, R.; Horima, S.; Sugimoto, H.; Chiba, A. A novel parallel motor winding structure for bearingless motors. *IEEE Trans. Magn.* **2013**, *49*, 2287–2290. [CrossRef]
35. Chiba, A.; Sotome, K.; Iiyama, Y.; Rahman, M.A. A novel middle-point-current-injection-type bearingless pm synchronous motor for vibration suppression. *IEEE Trans. Ind. Appl.* **2011**, *47*, 1700–1706. [CrossRef]
36. Petersen, N.P.; Severson, E.L. Rotor Eccentricity Impact on Electromagnetic Behavior in Combined Winding Bearingless Motors Towards Displacement Self-Sensing. *IEEE Trans. Energy Convers.* **2025**, *40*, 323–336. [CrossRef]
37. Petersen, N.; Khamitov, A.; Slininger, T.; Severson, E.L. Machine design and precision current regulation for the parallel DPNV bearingless motor winding. *IEEE Trans. Ind. Appl.* **2021**, *57*, 7000–7011. [CrossRef]
38. Silber, S.; Amrhein, W. Power optimal current control scheme for bearingless PM motors. In *Proceedings of the 7th International Symposium on Magnetic Bearings*; ETH Zurich: Zürich, Switzerland, 2000; pp. 401–406.
39. Khamitov, A.; Gruber, W.; Bramerdorfer, G.; Severson, E.L. Comparison of combined winding strategies for radial nonsalient bearingless machines. *IEEE Trans. Ind. Appl.* **2021**, *57*, 6856–6869. [CrossRef]
40. Anantachaisilp, P.; Lin, Z. An experimental study on PID tuning methods for active magnetic bearing systems. *Int. J. Adv. Mechatron. Syst.* **2013**, *5*, 146–154. [CrossRef]
41. Janhunen, S.; Mussalo, A. Modeling and PID-Control Design for Bearingless High Speed Motor Drive. Bachelor's Thesis, Lappeenranta University of Technology, Lappeenranta, Finland, 2018.
42. Han, J.; Li, Y.; Lin, Y.; Zhang, N.; Xiong, F. Research on tuning method of PID controller parameter for hybrid magnetic bearing. *J. Mech. Sci. Technol.* **2024**, *38*, 931–941. [CrossRef]
43. Petersen, N.P.; Severson, E.L. Tuning Methods for Classical SISO PID Magnetic Levitation Controllers via Analytic Models. In *Proceedings of the 18th International Symposium on Magnetic Bearings, ISMB*; Oxford University Press: Oxford, UK, 2023; pp. 1–6.
44. Nippatla, V.R.; Mandava, S. Performance analysis of permanent magnet synchronous motor based on transfer function model using PID controller tuned by Ziegler-Nichols method. *Results Eng.* **2025**, *26*, 105460. [CrossRef]
45. BOOSTXL-DRV8301 Evaluation Board. Available online: https://www.ti.com/tool/BOOSTXL-DRV8301 (accessed on 20 May 2026).

Disclaimer/Publisher's Note: The statements, opinions and data contained in all publications are solely those of the individual author(s) and contributor(s) and not of MDPI and/or the editor(s). MDPI and/or the editor(s) disclaim responsibility for any injury to people or property resulting from any ideas, methods, instructions or products referred to in the content.